Oxidative degradation of Orange G in aqueous solution by persulfate activated with pyrite

Xin Zhang, Yingzhi Qin, Weiting Zhang, Yali Zhang and Guang-En Yuan

ABSTRACT

Orange G (OG), a typical azo dye in textile wastewaters, has been the subject of intense investigations. This study investigated oxidative degradation of OG in aqueous solution by persulfate (PS) activated with pyrite. A complete destruction of OG was achieved within 60 min in the pyrite/PS system. Lower solution pH, smaller pyrite particles and higher pyrite dosage was beneficial for OG degradation. Higher PS concentration was also in favour of OG degradation, but excess PS would decrease the removal efficiency of OG. The addition of HCO_3^- and $H_2PO_4^-$ but Cl^- had inhibitory effects on the destruction of OG. The results of quenching experiments and electron paramagnetic resonance tests proved that $SO_4^{\bullet-}$ and •OH were the dominant reactive species responsible for OG degradation in the pyrite/PS system. The azo bond, naphthalene ring and benzene ring of OG were all destroyed by the generated reactive species. The mineralization rate of OG reached 34.4% after 60 min of reaction. This work will provide information for understanding azo dye degradation by pyrite activated PS.

Key words | mineralization, Orange G, persulfate, pyrite, sulfate radical

Xin Zhang (corresponding author)
Yingzhi Qin
Weiting Zhang
Yali Zhang
Guang-En Yuan
School of Environment,
Henan Normal University, Key Laboratory for Yellow River and Huai River Water Environmental and Pollution Control, Ministry of Education, Henan Key Laboratory for Environmental Pollution Control,
Xinxiang, Henan 453007,
China.
E-mail: *xinzhang2015@126.com*

HIGHLIGHTS

- Natural pyrite (FeS_2) was used to activate persulfate for OG degradation.
- A complete destruction of OG was achieved within 60 min in the pyrite/PS system.
- $SO_4^{\bullet-}$ and •OH were identified as the dominant reactive species responsible for OG degradation.
- The mineralization rate of OG reached 34.4% after 60 min of reaction.

INTRODUCTION

Large quantities of dye can be lost in water during dye production and their application, mainly in the textile and leather industry. Azo dyes make up almost 60% of the synthetic dyes used industrially, and most of them are recalcitrant, toxic and potentially carcinogenic in nature (Routoula & Patwardhan 2020). A variety of technologies, such as adsorption, biodegradation, ozonation, electrochemical oxidation and chemical reduction, are tried to remove azo dye from water, but these processes have high costs and limited applicability (Pavithra *et al.* 2019). Advanced oxidation processes (AOPs) were proposed as alternative technologies for treatment of refractory organic wastewater due to the high oxidizing ability of involved reactive species (Wang & Wang 2018).

In recent years, AOPs based on persulfate (PS) and permonosulfate (PMS) have found an increasingly wide utilization in environmental pollution control, especially for the treatment of biorefractory wastewater (Wang & Wang 2018). Sulfate radical ($SO_4^{\bullet-}$), a strong oxidizing agent (E° = 2.5–3.1 V vs. SHE), can be formed by PS and PMS with several activators, such as UV-light, transition metal ions (like Co^{2+}, Cu^{2+}, Ag^+, Fe^{2+} and Mn^{2+}), heat, carbon, and electrode (Wang & Wang 2018). Iron is the most widely used PS activator because it is effective, relatively non-toxic, environmentally friendly and more cost-effective than other transition metals. However, Fe^{2+}/PS system has the problems of rapid consumption of ferrous ion, narrow pH range and iron sludge production. To solve these problems, heterogeneous catalysts

doi: 10.2166/wst.2020.352

like zero-valent iron (Cao *et al.* 2019), goethite (Su *et al.* 2019), Fe_3O_4-sepiolite (Xu *et al.* 2019) and sulfide minerals (Chen *et al.* 2017; Lian *et al.* 2019) were developed. Among these heterogeneous catalysts, sulfide minerals hold great application prospects, because they could not only continually release Fe^{2+} ions to activate PS and PMS to produce $SO_4^{\cdot-}$ and hydroxyl radicals (•OH), but also promote the cycling of Fe^{3+}/Fe^{2+} couple with reducible sulfur in these minerals (Chen *et al.* 2017; Lian *et al.* 2019).

Orange G (OG), a typical azo dye in textile wastewaters, has been the subject of intense investigations. Several catalysts, such as ferrous ion (Xu & Li 2010), sewage sludge-derived magnetic nanocomposites (Li *et al.* 2017b) and iron-immobilized resin chars (Shi *et al.* 2015), have been used to activate PS for OG degradation. However, information about OG degradation by PS activated with sulfide minerals could not be found in the literature. In this study, pyrite (FeS_2), the most widely distributed sulfide in the earth's crust, was applied to degrade OG in aqueous solution in the presence of PS. Effects of various factors, initial solution pH, pyrite particle size, pyrite dosage, initial PS concentration and co-existing anions, were investigated. Reactive species responding for OG degradation in the pyrite/PS system were identified by quenching experiments and electron paramagnetic resonance (EPR) tests. The changes of Fe, O and S speciation during pyrite oxidation were characterized by X-ray photoelectron spectroscopy (XPS) and X-ray diffraction (XRD). The degradation intermediates of OG were analyzed with high resolution liquid chromatography quadropole time-of-flight mass spectrometry (LC-QTOF-MS), and its degradation pathway was proposed. Finally, the mineralization of OG in the pyrite/PS system was examined.

EXPERIMENTAL

Materials

Orange G (OG) with HPLC grade (>96%) was purchased from Shanghai Macklin Biochemical Co. Ltd, China. Potassium persulfate (PS, $Na_2S_2O_8$), methanol (MeOH, CH_3OH), tert-butyl alcohol (TBA, C_4H_9OH) and *p*-benzoquinone (BQ) were purchased from Sinopharm Group Chemical Reagent co. Ltd, China. All the above chemicals and reagents were of analytical grade and employed without further purification. Raw pyrite ore with high purity was purchased from Gaowantong Fossil Specimen Museum, Guilin, Guangxi Province, China. The raw ore was first milled with a ceramic mortar and sieved, and the resulting powder was then washed with 95% ethanol, 1 M HNO_3 and deionized water, successively. The as-prepared powder was finally dried at 30 °C and stored before use.

Experiments

All experiment reactions were operated on a magnetic stirrer with constant temperature water bath at a stirring rate of 150 rpm. Batch experiments were conducted in a 300 mL cylindrical glass container at 30 ± 0.5 °C. The container was covered with aluminium-foil paper to prevent the effect of light. OG aqueous solution was prepared by adding a certain amount of OG into deionized water. The experiments were started immediately after PS and pyrite were added into 200 mL OG aqueous solution successively. The pH was adjusted to desired values by 1 M H_2SO_4 or NaOH before adding pyrite into the solution. Samples (1.0 mL) were withdrawn at preselected time points, immediately quenched by 0.5 mL of methanol and filtrated with 0.45 μm membrane before analysis. Scavenging tests were conducted by adding a certain dose of MeOH, TBA or BQ to the reaction solution before the reaction started. Unless otherwise stated, the experimental conditions were set as $[PS]_0 = 5$ mM, $[pyrite]_0 = 1.0$ g/L, $pH_0 = 6.0$, $[OG]_0 = 100$ μM. Each experiment was performed in duplicate at least and the mean values were used for analysis. The error bars in the figures of the following contents represent standard deviation.

Analytical methods

The concentration of OG in aqueous solutions was determined by UV–vis spectrophotometry (752N, Shanghai INESA) at a maximum absorption wavelength of 478 nm. Solution pH was measured by a pH meter (PB-10, Sartorius). The concentration of Fe^{2+} was determined by spectrophotometric method with 1, 10-phenanthroline, and total dissolved Fe was also determined in the same way using hydroxylamine as the reducing agent. Total organic carbon (TOC) was measured by a TOC analyzer (Vario TOC Select, Germany). The degradation intermediates of OG were analyzed using LC-QTOF-MS. The mobile phase was 1 mM oxalic acid and acetonitrile aqueous solution, and the mass spectra were recorded across the range of 50–1,000 m/z with the negative scan mode.

The crystalline phase of the pyrite powder was determined by an X-ray powder diffractometer (XRD; X'Pert3 Powder, Netherlands Panaco) system equipped with Cu-Kα radiation source at 45 kV and 200 mA. The surface elements

of the pyrite powder was analyzed using X-ray photoelectron spectroscopy (XPS; ESCALAB250Xi, ThermoFisher) with monochromatized Al-Kα radiation. EPR tests were conducted on an EPR spectrometer (Bruker EMX 10/12, Bermen, Germany) to detect the generated active species, and 5,5-dimethy-1-pyrroline-N-oxide (DMPO) was chosen as spin-trapping reagent in the pyrite/PS system.

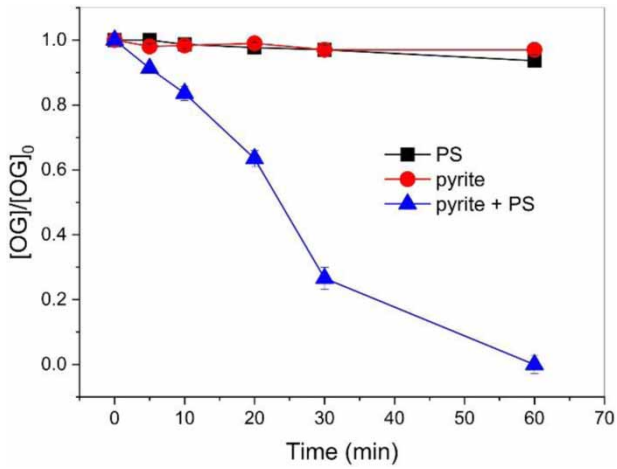

Figure 1 | Degradation of OG during different processes.

RESULTS AND DISCUSSION

OG degradation during different processes

As can be seen from Figure 1, 6.4% of OG was degraded in aqueous solution in 60 min by PS alone, suggesting that the oxidation of OG by PS alone was weak. It was reported that pyrite could degrade organic pollutants in the presence of O_2 (Zhang *et al.* 2015). However, the removal rate of OG was only 3.0% with pyrite alone, illustrating that pyrite had no obvious oxidative degradation and adsorption towards OG. On the contrary, the addition of pyrite and PS together to the solution resulted in a more rapid and prominent destruction of OG. The degradation rate of OG sped up from 20 min and then slowed down from 30 min, and the reasons may be the lower solution pH (seen from Figure 2(b)) and residual OG concentration in the later period of the reaction. OG was completely removed

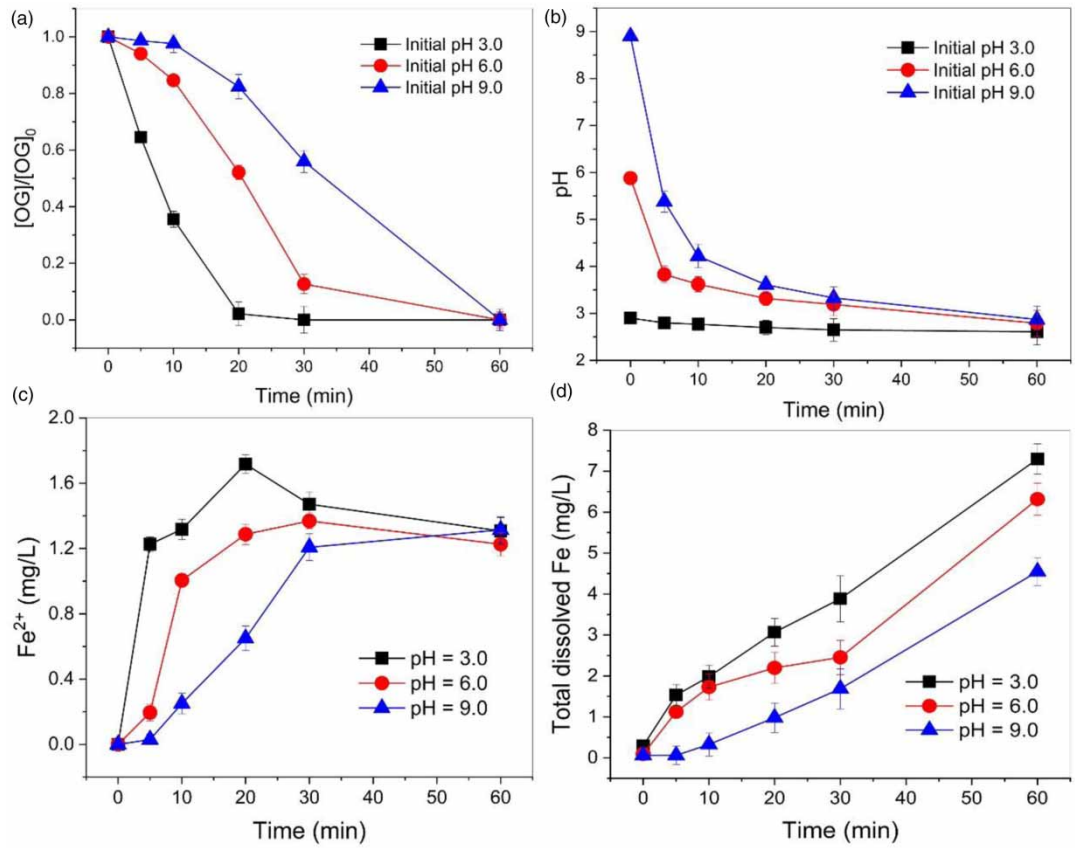

Figure 2 | Effects of initial solution pH on OG degradation in pyrite/PS system (a) and the changes of solution pH (b), Fe^{2+} concentration (c) and total dissolved Fe (d).

within 60 min, which indicated that pyrite could effectively activate PS for the degradation of organic pollutants. The rapid removal of OG may be attributed to the generated reactive species such as $SO_4^{\bullet-}$ and •OH by pyrite activated PS (seen from Figure 3).

Effects of initial solution pH

Effects of initial solution pH on OG degradation in the pyrite/PS system were examined. In general, low solution pH was beneficial to OG degradation (Figure 2(a)). For example, the removal rate of OG was 97.9% within the first 20 min at pH 3.0, which was much higher than those at pH 6.0 (47.9%) and 9.0 (17.6%). However, OG could be also completely removed even though the initial solution pH was at 9.0. In order to explain this phenomenon, the changes of solution pH, Fe^{2+} concentration and total dissolved Fe in the pyrite/PS system were determined. The solution pH decreased rapidly within the first 10 min and changed from 3.0, 6.0 and 9.0 to 2.61, 2.79 and 2.87 after 60 min of reaction, respectively (Figure 2(b)). This can be ascribed to two possible reasons. Firstly, H^+ ions were released when pyrite was oxidized by O_2, Fe^{3+} and PS (Equations (1)–(3)) (Zhang *et al.* 2017). Secondly, the generated $SO_4^{\bullet-}$ could be transformed into •OH, resulting in the consumption of OH^- or release of H^+ (Equations (4) and (5)) (Chen *et al.* 2017). The Fe^{2+} concentration all increased rapidly within the first 5 min at different initial pHs and soon afterwards tended to be stable (Figure 2(c)). The maximum concentration of Fe^{2+} at pH 3.0 was 1.72 mg/L, which was higher than those at pH 6.0 and 9.0. This illustrated that low solution pH was beneficial for continuous release of Fe^{2+} from pyrite, thus improving OG degradation. Total dissolved Fe in the pyrite/PS system all increased with the reaction time at different initial pHs (Figure 2(d)). The highest concentration of total dissolved Fe at initial pH 3.0, 6.0 and 9.0 were 7.30, 6.32 and 4.55 mg/L, respectively.

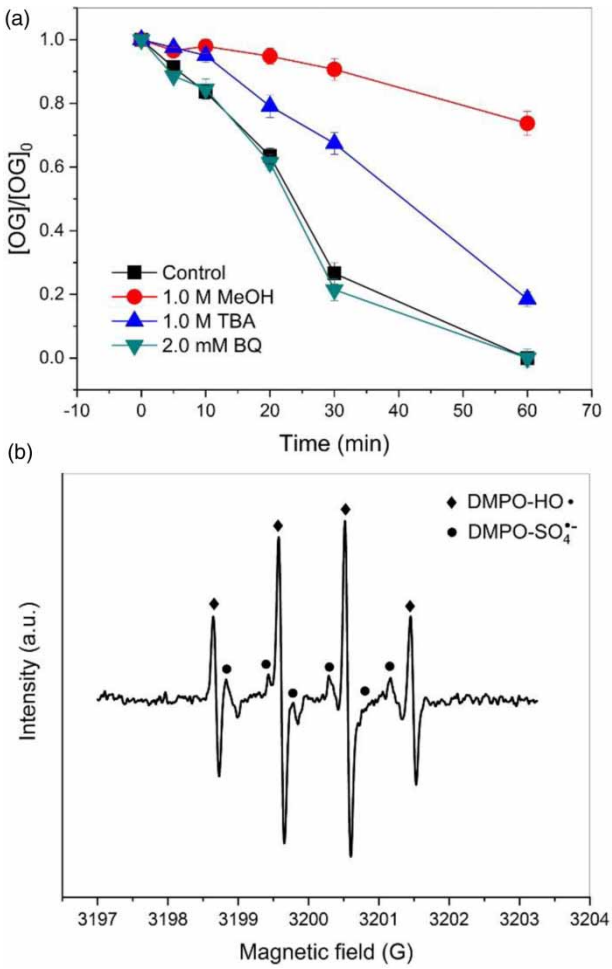

Figure 3 | Effect of quenchers on OG degradation (a) and EPR spectra of DMPO-HO•, DMPO-SO_4•$^-$ (b) in the pyrite/PS system.

$$2FeS_2 + 7O_2 + 2H_2O \rightarrow 2Fe^{2+} + 4SO_4^{2-} + 4H^+ \quad (1)$$

$$FeS_2 + 14Fe^{3+} + 8H_2O \rightarrow 15Fe^{2+} + 2SO_4^{2-} + 16H^+ \quad (2)$$

$$2FeS_2 + 15S_2O_8^{2-} + 16H_2O \rightarrow 2Fe^{3+} + 34SO_4^{2-} + 32H^+ \quad (3)$$

$$SO_4^{\bullet-} + OH^- \rightarrow \cdot OH + SO_4^{2-} \quad (4)$$

$$SO_4^{\bullet-} + H_2O \rightarrow \cdot OH + H^+ + SO_4^{2-} \quad (5)$$

Reactive species identification

Chemical scavengers were added into the solution before the reaction started to identify the involved reactive species such as $SO_4^{\bullet-}$, •OH and $O_2^{\bullet-}$. MeOH and TBA were frequently selected as chemical scavengers. MeOH which contains α-hydrogen can quench both $SO_4^{\bullet-}$ and •OH with the rate constants of 1.6×10^7 and $1.9 \times 10^9\ M^{-1}\ S^{-1}$, whereas TBA is often used as a more effective scavenger for •OH, because its rate constant with $SO_4^{\bullet-}$ ($4.0 \times 10^5\ M^{-1}\ S^{-1}$) is much lower than that with •OH ($6.0 \times 10^8\ M^{-1}\ S^{-1}$) (Fu *et al.* 2019). BQ has been demonstrated to be an efficient scavenger for $O_2^{\bullet-}$ ($9.6 \times 10^8\ M^{-1}\ S^{-1}$) (Wang *et al.* 2018). Effect of MeOH, TBA and BQ on OG degradation in the pyrite/PS system were displayed in Figure 3(a). Significant inhibitory effects on OG degradation were observed after the addition of 1.0 M MeOH and 1.0 M

TBA, and the inhibitory effect of MeOH was much more stronger than that of TBA, suggesting that both $SO_4^{\bullet-}$ and •OH were the dominant reactive species and had played important roles in the degradation process. No obvious inhibition effect was observed with the addition of 2.0 mM BQ, indicating that $O_2^{\bullet-}$ contributed little to OG degradation. EPR technique was used to further identify the generated reactive species. As shown in Figure 3(b), the signals assigned to DMPO-HO• and DMPO-$SO_4^{\bullet-}$ adducts were detected in the pyrite/PS system. This verified it was $SO_4^{\bullet-}$ and •OH that were the dominant reactive species responsible for OG degradation.

Effects of pyrite particle size, pyrite dosage, PS concentration and co-existing inorganic anions

Effects of pyrite particle size, pyrite dosage, PS concentration and co-existing anions on OG degradation are presented in the Figure 4. Pyrite particle size had a remarkable impact on the degradation rate of OG (Figure 4(a)). Complete destruction of OG was obtained within 20, 60 and 90 min for the pyrite particle size of 300, 180–300 and 80–180 Mesh, respectively. This is because smaller pyrite particles possessed higher total surface area and would released more dissolved ferrous ions to activate PS (Zhang *et al.* 2017). The decomposition rate of OG increased with the increase of pyrite dosage (Figure 4(b)). The removal rates of OG were 19.4 and 60.8% for pyrite dosages of 0.25 and 0.5 g/L, and OG could be completely degraded in 60, 30 and 20 min for pyrite dosages of 1.0, 1.5 and 2.0 g/L, respectively. These suggested that pyrite served as an ≡Fe(II) or Fe^{2+} source for PS activation. Higher PS concentration was in favour of OG degradation, but excess PS would decrease the removal efficiency of OG (Figure 4(c)). This is because PS not only was the source of active radicals but also could act as the radical scavenger (Chen *et al.* 2017). Effects of co-existing inorganic anions on OG destruction were

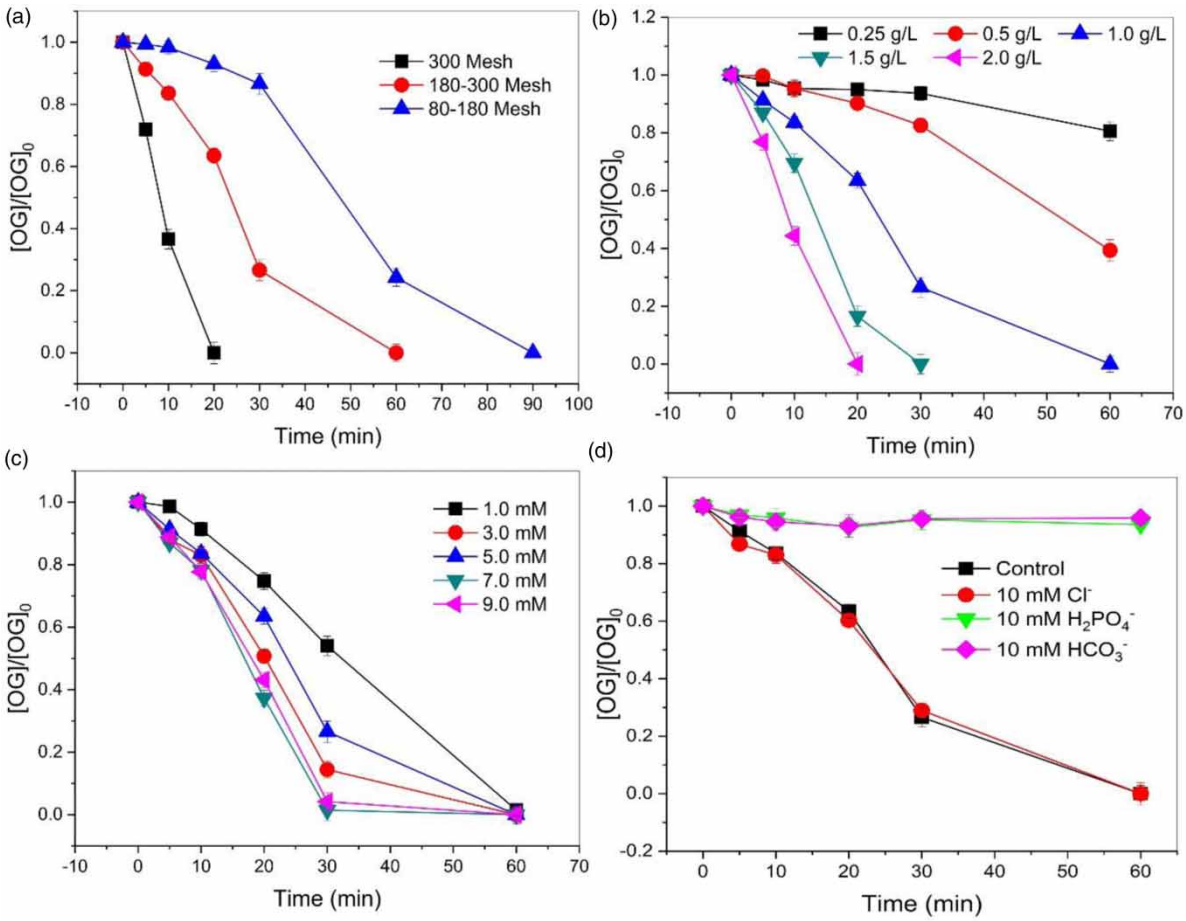

Figure 4 | Effects of pyrite particle size (a), pyrite dosage (b), PS concentration (c) and co-existing inorganic anions (d) on OG degradation.

depicted in Figure 4(d). Notably, the addition HCO_3^- and $H_2PO_4^-$ all had inhibitory effects on the destruction of OG. This may be because the generated $SO_4^{\bullet-}$ or •OH were transformed into weaker radical species such as $CO_3^{\bullet-}$ and $HPO_4^{\bullet-}$ (Equations (6) and (7)), thus reducing the degradation efficiency of OG (Li *et al.* 2017a; Peng *et al.* 2018). The generated reactive species could also react with Cl^- forming weaker radical species such as Cl•, ClHO• and $Cl_2^{\bullet-}$, but the addition of Cl^- had no inhibitory effect on OG degradation. This may be because active chlorine could also oxidize azo dye effectively in the presence of iron ion (Aguilar *et al.* 2017).

$$SO_4^{\bullet-}(\cdot OH) + HCO_3^- \rightarrow CO_3^{\bullet-} + HSO_4^-(OH^-) \quad (6)$$

$$SO_4^{\bullet-}(\cdot OH) + H_2PO_4^- \rightarrow HPO_4^{\bullet-} + HSO_4^-(OH^-) \quad (7)$$

Characterizations of the fresh and used pyrite

Figure 5(a) shows XRD pattern of the fresh and used pyrite at 2-Theta values from 20 to 90°. The sharpness of XRD reflections clearly illustrated that the fresh pyrite was highly crystalline. The XRD pattern of the fresh and used pyrite matched well with the standard XRD data of pyrite (JCPDF: 42-1340), which demonstrated that the main component of pyrite was FeS_2 and its crystal structure was not destructed after used.

To explore the elemental composition and the surface electronic states of pyrite, XPS spectroscopy was further performed. As shown in Figure 5(b), the fresh pyrite was mainly composed of Fe, S, C, O and Al elements. The detection of C and O may be caused by the adsorption of amorphous C and O on the sample in contact with air and some nonmetal and metal (such as Si, Mg and Al) oxide on the surface of pyrite. After used, Fe and S on the surface of pyrite were

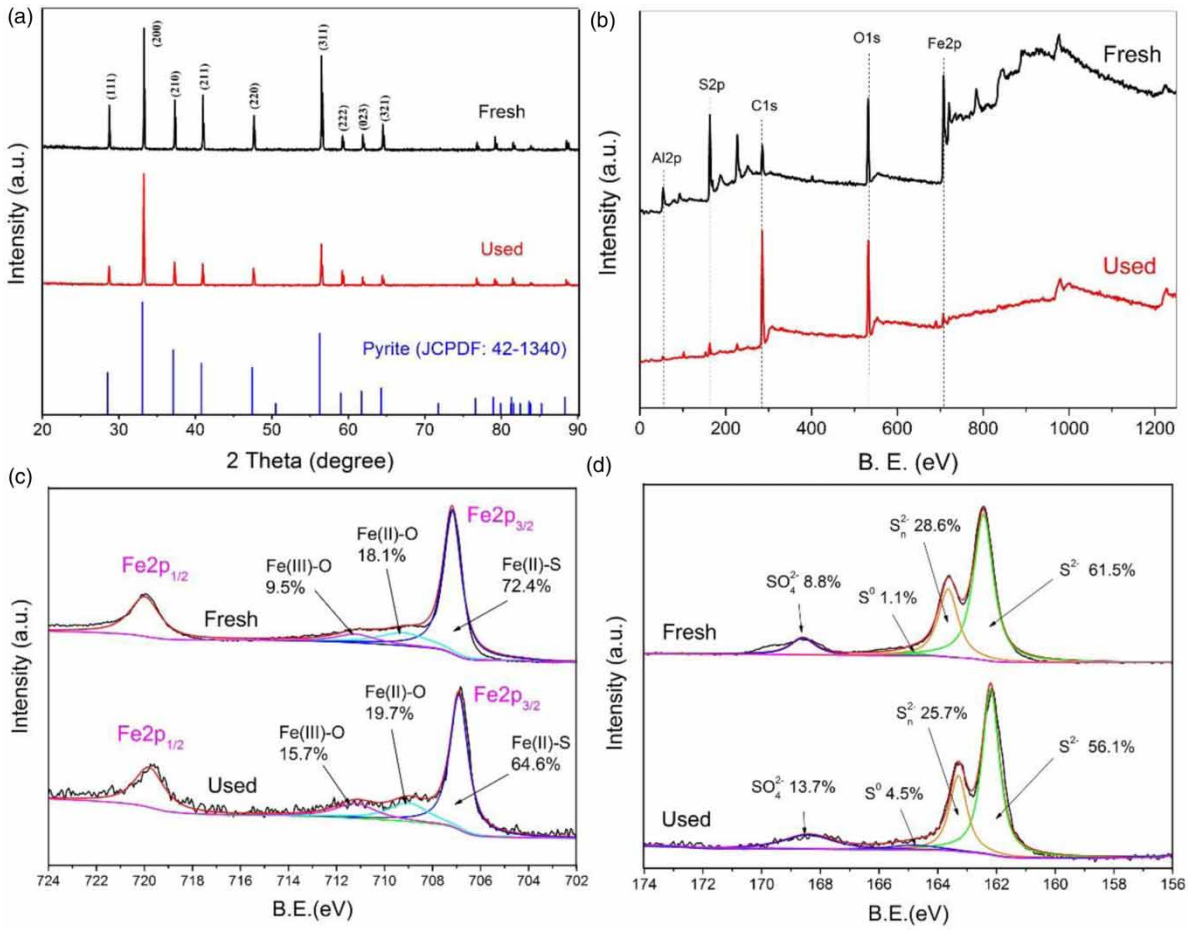

Figure 5 | Characterization of the fresh and used pyrite. XRD spectra (a); XPS survey spectra (b); XPS high-resolution Fe 2p (c); XPS high-resolution S 2p (d).

significantly reduced, and the reason might be that these elements were oxidized and then released into aqueous phase. Figure 5(c) showed the high-resolution Fe 2p spectra of the fresh and used pyrite. There were two peaks at 724.8 eV and 711.2 eV, which corresponded to Fe $2p_{1/2}$ and Fe $2p_{3/2}$, respectively, and were characteristic of Fe(II) and Fe(III) on the surface of pyrite (Xia *et al.* 2018). Satellites of Fe(II) and Fe(III) at 715.0 and 719.9 eV were also found in the Fe 2p spectra of the fresh and used pyrite. Clearly, the proportion of Fe(II) species on the surface of pyrite declined from 72.4 to 64.6% after used, indicating the oxidation of Fe(II) into Fe(III) species on the surface of pyrite. The high-resolution S 2p spectra of the fresh and used pyrite are shown in Figure 5(d), and the bonding energies at 162.4, 163.6, 164.8 and 168.6 eV originated from the monosulfide (S^{2-}), polysulfide (S_n^{2-}), elemental sulfur (S^0)

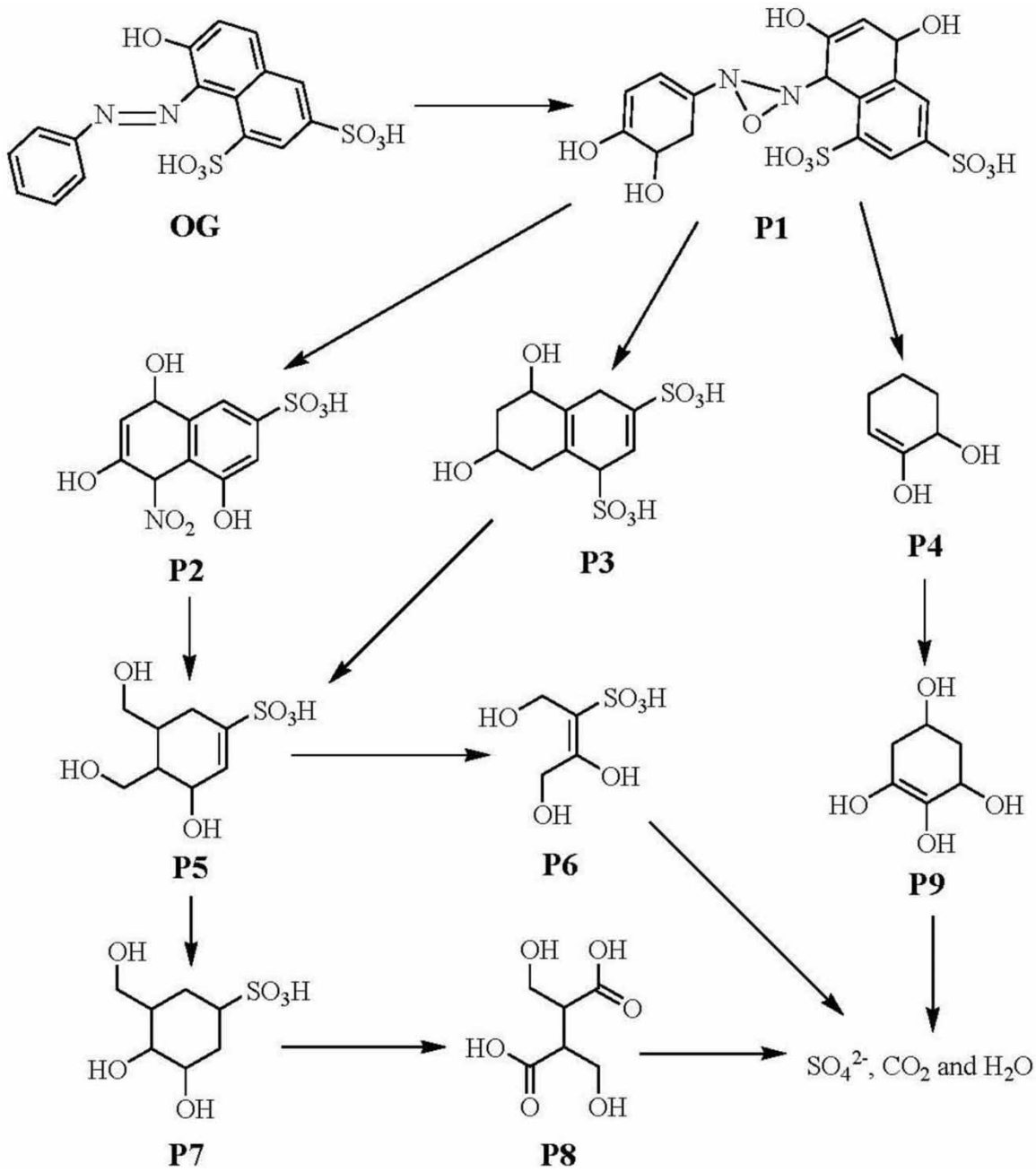

Figure 6 | The proposed degradation pathway of OG in the pyrite/PS system.

and sulfate (SO_4^{2-}), respectively. The percentages of S^{2-}, S_n^{2-}, S^0 and SO_4^{2-} species on the surface of the fresh pyrite catalyst were 61.5, 28.6, 1.1 and 8.8%, respectively. After used, the percentages of these sulfur species changed to 56.1, 25.7, 4.5, and 13.7%, respectively. This means that S^{2-} and S_n^{2-} in the pyrite were oxidized into S^0 and SO_4^{2-} in the oxidation process, which is in good accord with other reports (Zhang *et al.* 2017; Fan *et al.* 2018). It was believed that reducible sulfur in sulfide minerals could convert Fe^{3+} back into Fe^{2+} and then improve PS activation (Zhang *et al.* 2017; Zhou *et al.* 2018). Our previous study also verified reductive sulfur in sulfide minerals could enhance the regeneration of Fe^{2+} and thus promote the degradation efficiency of organic pollutants by activated PS (Zhang *et al.* 2020). Therefore, we presumed that reductive sulfur in pyrite in this work accelerated Fe^{3+}/Fe^{2+} cycle and thus OG degradation, which could be seen in Figure 2(c), where Fe^{2+} stabilized at a certain concentration instead of depletion in the later reaction period.

Degradation intermediates and pathway of OG

The degradation intermediates of OG were analyzed using LC-QTOF-MS. Figure S1 shows the liquid chromatograms and the corresponding mass spectra of the OG solution at the reaction time of 20 min. The degradation intermediates of OG meanly included nine compounds and their potential molecular structures are listed in Table S1. The degradation pathway of OG in the pyrite/PS system is proposed in Figure 6. The azo bond of OG was first attacked by active species via epoxidation, and simultaneously the benzene ring and naphthalene ring of OG were oxidized through hydroxylation, resulting the formation of intermediate **P1**. The intermediate **P1** was then transformed into **P2**, **P3** and **P4** through the cleavage of the N – N bond, denitrogenation and desulfonation. **P4** was then oxidized into **P9** and finally mineralized into CO_2 and H_2O. **P5** could be obtained from **P2** and **P3** via processes like ring-opening, decarbonylation and hydroxylation, and it was further oxidized into **P6**, **P7** and **P8**, which were subsequently mineralized into SO_4^{2-}, CO_2 and H_2O.

The mineralization of OG

The concentration of TOC was measured to determine the degree of OG mineralization in the pyrite/PS system. As shown in Figure 7, the removal rate of TOC increased with the reaction time and reached a maximum value of 34.4%. The mineralization rate of OG was much slower than its degradation rate, and the effluent of the pyrite/PS system must be further treated. As we known, azo dyes are xenobiotic compounds, and they are difficult to degrade by aerobic biological method due to the electron withdrawing nature of the azo bond. Combination of AOPs and biological processes are often applied for industrial textile wastewater treatment, and AOPs could improve the biodegradability prior to biological treatment (Paździor *et al.* 2019). Thus, the pyrite/PS system can be used as pretreatment for azo dye wastewater.

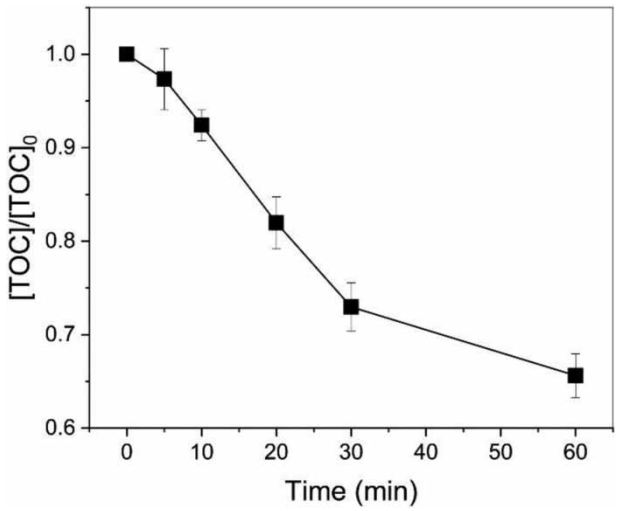

Figure 7 | The mineralization of OG in the pyrite/PS system.

CONCLUSIONS

Pyrite could effectively activate PS for the degradation of OG in aqueous solution, and a complete destruction of OG was achieved within 60 min. Lower solution pH, smaller pyrite particles and higher pyrite dosage were beneficial for OG degradation. Higher PS concentration was in favour of OG degradation, but excess PS would decrease the removal efficiency of OG. The addition of HCO_3^- and $H_2PO_4^-$ but Cl^- had inhibitory effects on the destruction of OG. $SO_4^{\bullet-}$ and •OH were the dominant reactive species responsible for OG degradation in the pyrite/PS system. The azo bond, naphthalene ring and benzene ring of OG were all destroyed by the generated reactive species. The mineralization rate of OG in the pyrite/PS system was only 34.4% after 60 min of reaction. The pyrite/PS system can be used to treat azo dye wastewater or as pretreatment method to improve its biodegradability.

DATA AVAILABILITY STATEMENT

All relevant data are included in the paper or its Supplementary Information.

REFERENCES

Aguilar, Z. G., Brillas, E., Salazar, M., Nava, J. L. & Sirés, I. 2017 Evidence of Fenton-like reaction with active chlorine during the electrocatalytic oxidation of Acid Yellow 36 azo dye with Ir-Sn-Sb oxide anode in the presence of iron ion. *Applied Catalysis B: Environmental* **206**, 44–52.

Cao, J., Lai, L., Lai, B., Yao, G., Chen, X. & Song, L. 2019 Degradation of tetracycline by peroxymonosulfate activated with zero-valent iron: performance, intermediates, toxicity and mechanism. *Chemical Engineering Journal* **364**, 45–56.

Chen, H., Zhang, Z., Feng, M., Liu, W., Wang, W., Yang, Q. & Hu, Y. 2017 Degradation of 2,4-dichlorophenoxyacetic acid in water by persulfate activated with FeS (mackinawite). *Chemical Engineering Journal* **313**, 498–507.

Fan, J., Gu, L., Wu, D. & Liu, Z. 2018 Mackinawite (FeS) activation of persulfate for the degradation of p-chloroaniline: surface reaction mechanism and sulfur-mediated cycling of iron species. *Chemical Engineering Journal* **333**, 657–664.

Fu, H., Ma, S., Zhao, P., Xu, S. & Zhan, S. 2019 Activation of peroxymonosulfate by graphitized hierarchical porous biochar and $MnFe_2O_4$ magnetic nanoarchitecture for organic pollutants degradation: structure dependence and mechanism. *Chemical Engineering Journal* **360**, 157–170.

Li, W., Orozco, R., Camargos, N. & Liu, H. 2017a Mechanisms on the impacts of alkalinity, pH, and chloride on persulfate-based groundwater remediation. *Environmental Science & Technology* **51** (7), 3948–3959.

Li, Y., Yang, Z., Zhang, H., Tong, X. & Feng, J. 2017b Fabrication of sewage sludge-derived magnetic nanocomposites as heterogeneous catalyst for persulfate activation of Orange G degradation. *Colloids and Surfaces A: Physicochemical and Engineering Aspects* **529**, 856–863.

Lian, W., Yi, X., Huang, K., Tang, T., Wang, R., Tao, X., Zheng, Z., Dang, Z., Yin, H. & Lu, G. 2019 Degradation of tris(2-chloroethyl) phosphate (TCEP) in aqueous solution by using pyrite activating persulfate to produce radicals. *Ecotoxicology and Environmental Safety* **174**, 667–674.

Pavithra, K. G., Senthil Kumar, P., Jaikumar, V. & Sundar Rajan, P. 2019 Removal of colorants from wastewater: a review on sources and treatment strategies. *Journal of Industrial and Engineering Chemistry* **75**, 1–19.

Paździor, K., Bilińska, L. & Ledakowicz, S. 2019 A review of the existing and emerging technologies in the combination of AOPs and biological processes in industrial textile wastewater treatment. *Chemical Engineering Journal* **376**, 120597.

Peng, J., Lu, X., Jiang, X., Zhang, Y., Chen, Q., Lai, B. & Yao, G. 2018 Degradation of atrazine by persulfate activation with copper sulfide (CuS): kinetics study, degradation pathways and mechanism. *Chemical Engineering Journal* **354**, 740–752.

Routoula, E. & Patwardhan, S. V. 2020 Degradation of anthraquinone dyes from effluents: a review focusing on enzymatic dye degradation with industrial potential. *Environmental Science & Technology* **54** (2), 647–664.

Shi, Q., Li, A., Qing, Z. & Li, Y. 2015 Oxidative degradation of Orange G by persulfate activated with iron-immobilized resin chars. *Journal of Industrial and Engineering Chemistry* **25**, 308–313.

Su, S., Cao, C., Zhao, Y. & Dionysiou, D. D. 2019 Efficient transformation and elimination of roxarsone and its metabolites by a new α-FeOOH@GCA activating persulfate system under UV irradiation with subsequent As(V) recovery. *Applied Catalysis B: Environmental* **245**, 207–219.

Wang, J. & Wang, S. 2018 Activation of persulfate (PS) and peroxymonosulfate (PMS) and application for the degradation of emerging contaminants. *Chemical Engineering Journal* **334**, 1502–1517.

Wang, Q., Wang, B., Ma, Y. & Xing, S. 2018 Enhanced superoxide radical production for ofloxacin removal via persulfate activation with Cu-Fe oxide. *Chemical Engineering Journal* **354**, 473–480.

Xia, D., He, H., Liu, H., Wang, Y., Zhang, Q., Li, Y., Lu, A., He, C. & Wong, P. K. 2018 Persulfate-mediated catalytic and photocatalytic bacterial inactivation by magnetic natural ilmenite. *Applied Catalysis B: Environmental* **238**, 70–81.

Xu, X.-R. & Li, X.-Z. 2010 Degradation of azo dye Orange G in aqueous solutions by persulfate with ferrous ion. *Separation and Purification Technology* **72** (1), 105–111.

Xu, X., Chen, W., Zong, S., Ren, X. & Liu, D. 2019 Atrazine degradation using Fe_3O_4-sepiolite catalyzed persulfate: reactivity, mechanism and stability. *Journal of Hazardous Materials* **377**, 62–69.

Zhang, Y., Tran, H. P., Hussain, I., Zhong, Y. & Huang, S. 2015 Degradation of p-chloroaniline by pyrite in aqueous solutions. *Chemical Engineering Journal* **279**, 396–401.

Zhang, Y., Tran, H. P., Du, X., Hussain, I., Huang, S., Zhou, S. & Wen, W. 2017 Efficient pyrite activating persulfate process for degradation of p-chloroaniline in aqueous systems: a mechanistic study. *Chemical Engineering Journal* **308**, 1112–1119.

Zhang, X., Deng, H., Zhang, G., Yang, F. & Yuan, G.-E. 2020 Natural bornite as an efficient and cost-effective persulfate activator for degradation of tetracycline: performance and mechanism. *Chemical Engineering Journal* **381**, 122717.

Zhou, Y., Wang, X., Zhu, C., Dionysiou, D. D., Zhao, G., Fang, G. & Zhou, D. 2018 New insight into the mechanism of peroxymonosulfate activation by sulfur-containing minerals: role of sulfur conversion in sulfate radical generation. *Water Research* **142**, 208–216.

First received 14 April 2020; accepted in revised form 16 July 2020. Available online 29 July 2020